



HAL
open science

Global warming at near-constant tropospheric relative humidity is supported by observations

Hervé Douville, Saïd Qasmi, Aurélien Ribes, Olivier Bock

► **To cite this version:**

Hervé Douville, Saïd Qasmi, Aurélien Ribes, Olivier Bock. Global warming at near-constant tropospheric relative humidity is supported by observations. *Communications Earth & Environment*, 2022, 3, 10.1038/s43247-022-00561-z . insu-03824245

HAL Id: insu-03824245

<https://insu.hal.science/insu-03824245>

Submitted on 21 Oct 2022

HAL is a multi-disciplinary open access archive for the deposit and dissemination of scientific research documents, whether they are published or not. The documents may come from teaching and research institutions in France or abroad, or from public or private research centers.

L'archive ouverte pluridisciplinaire **HAL**, est destinée au dépôt et à la diffusion de documents scientifiques de niveau recherche, publiés ou non, émanant des établissements d'enseignement et de recherche français ou étrangers, des laboratoires publics ou privés.



Distributed under a Creative Commons Attribution 4.0 International License

Global warming at near-constant tropospheric relative humidity is supported by observations

Hervé Douville ¹✉, Saïd Qasmi ¹, Aurélien Ribes¹ & Olivier Bock ^{2,3}

Although global warming is expected to occur at approximately constant relative humidity, the latest IPCC report remains elusive about the magnitude of observed changes in tropospheric humidity and their attribution. Here we use a quality-controlled dataset of in situ observations, global reanalyses, and a long record of global mean surface temperature to constrain both recent and future changes in global mean total precipitable water. Most state-of-the-art global climate models tend to exaggerate the projected atmospheric moistening, in line with their overestimation of global warming and of the sensitivity of atmospheric humidity to both anthropogenic greenhouse gases and aerosols across the 20th century. A 39% narrowing in the range of the projections is obtained after applying the observational constraints, with a best-guess estimate of +7% per °C of global warming. This finding provides further evidence of a substantial intensification of the global water cycle as long as global warming continues.

¹CNRM, Université de Toulouse, Météo-France, CNRS, Toulouse, France. ²Université Paris Cité, IPGP, CNRS, IGN, F-75005 Paris, France. ³ENSG-Géomatique, IGN, F-77455 Marne-la-Vallée, France. ✉email: herve.douville@meteo.fr

Global warming is expected to intensify the global water cycle^{1–3}, including the magnitude of heavy precipitation and related extremes^{3–5}. This adverse hydrological response is grounded in the Clausius-Clapeyron (CC) relationship, which indicates that the water holding capacity of air increases by about 7% per 1 °C of warming, at least in the lower troposphere where most of the atmospheric water vapour resides. Moreover, global warming is generally assumed to occur at near-constant relative humidity^{2,6}. In other words, a common hypothesis is that CC does not only control the size of the atmospheric water reservoir but also its content on climate change timescales. As a result, water vapour changes represent a major positive feedback in climate projections and can thus contribute to the inter-model spread in climate sensitivity^{7,8}. Water vapour also modulates the horizontal moisture transport and, thereby, the global water cycle intensity^{1,2} and related precipitation extremes^{3,4}. While all global climate models support the constant tropospheric relative humidity hypothesis, they still disagree on the quantitative water cycle response to anthropogenic radiative forcings^{3,7}, which may challenge their ability to predict accurately the global mean total precipitable water (GTPW) response to global warming. Their limited horizontal resolution for instance requires the use of empirical sub-grid parametrizations which can be responsible for model biases but also for contrasted hydrological sensitivities. More importantly, the theoretical expectation of a global warming at constant tropospheric relative humidity is still lacking an unequivocal observational evidence.

Total precipitable water or the total column of water vapour is defined as the mass of water vapour in an atmospheric column over a unit area (kg/m^2). It should be distinguished from the near-surface humidity whose response to global warming is not uniform between land and sea⁹ and not necessarily indicative of the whole total water vapor column¹⁰. While GTPW is a relevant indicator of climate change, global atmospheric reanalyses do not show fully consistent variations due to the use of evolving satellite data and the lack of homogeneity in the assimilated observations¹¹. Several satellite missions have been launched to provide a quasi-global assessment of total precipitable water, but failed to provide consistent trend estimates despite an overall tropical moistening on top of the strong influence of the El Niño Southern Oscillation variability. Most products exhibit apparent breakpoints, which are generally coincident with changes in the observing system¹¹. Even the most recent reanalyses, such as the ECMWF Retrospective Analysis (ERA5) and the NASA Modern-Era Retrospective Analysis for Research and Applications version 2 (MERRA-2) still suffer from spurious water cycle shifts, not only due to the assimilation of inhomogeneous radiance satellite data¹¹ but also to changes in the surface-wind observing system¹².

Since 2010, the Global Climate Observing System (GCOS) declared the total column water vapour to be an essential climate variable and emphasized the need of long and homogeneous time series for the detection and attribution (D&A) of both local and global changes. Yet, only few formal D&A studies have been published so far regarding the recent increase in atmospheric humidity^{13–15}. The only formal study on the vertically-integrated water vapour content was based on the third generation of global climate models (CMIP3) and a relatively short (1988–2007) satellite record of microwave measurements above ocean only¹³. The focus has been also on land surface humidity¹⁵, with a suggested underestimation of the observed drying in most previous-generation GCMs^{16,17}. The lack of reliable observational evidence has hampered recent progress in the assessment of GTPW trends from the fifth to the sixth Assessment Report of the IPCC. The AR5 concluded that total column water vapour very likely increased since the 1970s at a rate that is overall consistent

with the CC relationship (about 7%/°C), and that an anthropogenic contribution to increases in specific humidity was found with medium confidence at and near the surface. The AR6⁷ was even more cautious, stating only that (it is likely that) human influence has contributed to moistening in the upper troposphere since 1979¹⁸.

Here, and for the first time to the best of our knowledge, we use a quality-controlled dataset of in situ measurements, as well as reanalyses and multiple estimates of the historical global warming, to constrain the projections of GTPW from two generations of global climate models (GCMs). The results provide further and stronger evidence that human-induced global warming occurs at near-constant tropospheric relative humidity, with a substantial narrowing of the projected changes in GTPW regardless the explored emission scenario or GCM generation.

Results and Discussion

Since the early 1990s, ground-based measurements from the Global Navigation Satellite Systems (GNSS) have been shown to enable the estimation of total-column water vapour by applying the technique of accurate positioning¹⁹. They supplement the global radiosonde observations and provide an alternative and potentially more reliable reference for the evaluation of satellite retrieval algorithms and of global atmospheric models^{20,21}. GNSS measurements are not sensitive to weather conditions and are performed with high temporal resolutions (typically a few minutes). The technique consists in the retrieval of the vertically integrated water vapour column from propagation delay measurements. It is relatively insensitive to instrumentation changes and is thus suitable for trend assessments²².

The present study takes advantage of a recently updated GNSS dataset²³ based on a network of 434 stations with more or less continuous measurements from January 1994 to December 2021. These stations exhibit globally averaged anomalies that are consistent with the global mean values derived from several state-of-the-art atmospheric reanalyses over recent decades (Fig. 1). The estimated linear trends since 1994 are also fairly consistent. ERA5 shows a slightly stronger global moistening ($+0.39 \text{ kg m}^{-2} \text{ decade}^{-1}$) than GNSS ($+0.34 \text{ kg m}^{-2} \text{ decade}^{-1}$) and the other two reanalyses ($+0.32$ and $+0.33 \text{ kg m}^{-2} \text{ decade}^{-1}$), but these differences are not statistically significant given the $0.06 \text{ kg m}^{-2} \text{ decade}^{-1}$ standard error. The 20th century reanalyses from ECMWF (ERA20C²⁴) is also consistent with the other products, although it only assimilates surface pressure and surface wind measurements. This result indicates that GTPW is strongly constrained by the prescribed boundary conditions of observed sea surface temperature. It also suggests that the pre-1994 stalling of GTPW found in ERA5, MERRA-2 and JRA55 is likely an artifact of changes in the observation system. This hypothesis is further supported by a recent study¹⁰ which considered the pre-1994 decreases in low-altitude tropical water vapor from ERA5 suspect based on inconsistency with simulations and microwave satellite data since 1979. For this reason, we will only use the 1994–2021 observation period to constrain the climate projections. ERA20C will not be used as a direct observational constraint, but will be used indirectly (via a simple regression technique, see Methods) to derive GTPW anomalies from the observed variations in global mean surface air temperature (GSAT).

Beyond observations and reanalyses, the latest-generation GCMs from CMIP6 can be also used to document and better understand the historical evolution of GTPW (Fig. 2). Four multi-model ensembles of 1850–2020 simulations achieved in the framework of the DAMIP project²⁵ can be compared: hist-NAT (natural forcings only), hist-GHG (anthropogenic greenhouse

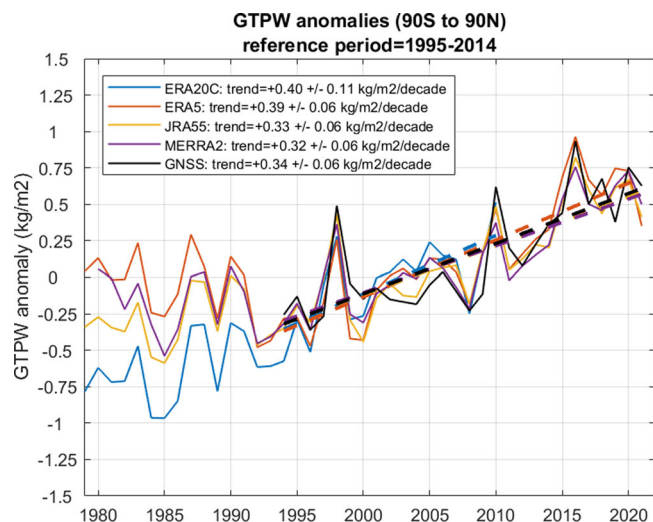


Fig. 1 Recent trends in global mean total precipitable water. Annual mean timeseries (1980–2021) of global mean total precipitable water (GTPW) from ground-based GNSS measurements of GPS reception and from four global atmospheric reanalyses (ERA5, ERA20C, JRA55 and MERRA-2). Anomalies have been estimated against the 1995–2014 reference climatology, except for ERA20C (1995–2010) which does not extend beyond 2010. Linear trends have been estimated over the 1994–2021 period (only 1994–2010 for ERA20C) using a generalized least-squares method with errors modelled as a first-order auto-regressive process. The estimated trends are reported with ± 1 standard error.

gases only), hist-AER (anthropogenic aerosols only), and hist-ALL (all historical forcings, also including a few other forcings in some but not all models, such as land-use change). Only eight CMIP6 models providing a minimum of three realizations for each experiment have been considered (see Methods). The hist-ALL ensemble shows an overall increase in GTPW since the mid-19th century, which is broadly consistent with the poorly constrained ERA20C reanalysis that only assimilates surface pressure and surface wind measurements. Remarkably, the simulated increase is much stronger after the mid-1980s, and is quite consistent with the GNSS measurements from 1994 to 2021. This result suggests a substantial influence of the anthropogenic emissions of sulphate aerosols, which peaked in the mid-1980s before declining at the global scale^{3,7}.

Parallel historical experiments with individual radiative forcings confirm this hypothesis. The 20th century GTPW response is mainly the combination of a strong water cycle sensitivity to both GHG and AER forcings, with the latter damping the atmospheric moistening caused by GHG emissions. Compared to human activities, natural forcings (i.e., solar activity and volcanic eruptions) and internal variability (as assessed from the multi-member ensembles) only had a marginal influence. The key role of anthropogenic aerosols in damping the early GTPW response to GHG is consistent with our current understanding of the water cycle sensitivity^{3,26}. Similar conclusions have been drawn for the response of GSAT²⁷, in line with the AR6 highlighting that the observed global warming of ~ 1.1 °C since the late 19th century is unequivocally attributable to a human influence^{18,27}.

While the ensemble-mean response of the subset of eight CMIP6 models is quite consistent with the GNSS measurements, there is a substantial range of historical responses across individual models (cf. shading in Fig. 2). The spread is even more pronounced in 21st century projections, where many more models can be used to assess future changes in GTPW. Our focus is first on the SSP2-4.5 scenario whose early GHG emissions are fairly consistent with the observed trends. All projections (2015–

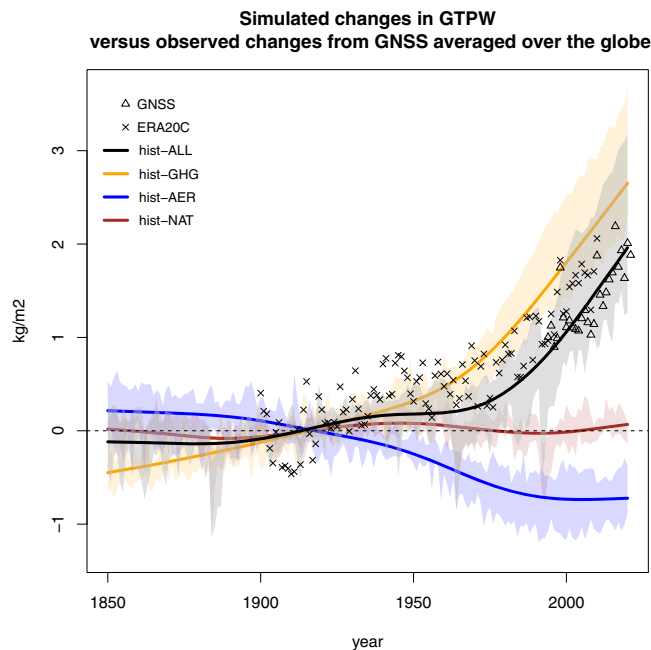


Fig. 2 Attribution of observed changes in global mean total precipitable water. Annual mean timeseries (1850–2020) of global mean anomalies of total precipitable water (GTPW) from four sets of historical experiments using a subset of eight CMIP6 models with at least three realization for each set of experiment driven by individual anthropogenic (GHG, AER) or natural (NAT) radiative forcings or their combination (ALL). ERA20C (crosses) and GNSS (triangles) anomalies are also shown as observational references. All anomalies are estimated relative to the 1900–1929 baseline period. Since GNSS measurements are only available since 1994, the anomalies shown in Fig. 1 have been shifted using the 1995–2014 minus 1900–1929 climatological differences from the historical simulations with ALL forcings. A spline smoothing with 6 degrees of freedom has been applied to the ensemble mean anomalies.

2100) have been concatenated to their corresponding historical simulations (1850–2014). GSAT and GTPW annual anomalies have been estimated against the 1995–2014 baseline period and show a substantial range across the 21st century (Supplementary Fig. 1a, b). Beyond the raw CMIP6 model distribution, another range of GTPW responses has been derived by assuming that all models follow a simple CC scaling (see Methods). This scaling is obtained by regressing the anomalies of $\ln[\text{GTPW}]$ onto the corresponding anomalies of GSAT. The regression fit is first estimated on simulated annual mean anomalies over the 1900–2010 period (Supplementary Fig. 1c). The predicted range and ensemble mean match the raw GTPW distribution, thereby confirming that most CMIP6 models comply with this simple scaling. An ERA20C-constrained regression coefficient ($7.8\%/^{\circ}\text{C}$) can be then estimated over the same period, and used to predict the simulated GTPW anomalies from the global warming of each CMIP6 model (Supplementary Fig. 1d). This empirical constraint leads to an upward shift of the projected distribution, which can be explained by a lower ensemble mean regression coefficient ($6.9\%/^{\circ}\text{C}$) in the CMIP6 models over the same training period. This result should be however considered with great caution for at least three reasons: i) the assumed time-scale invariance of the GTPW-GSAT relationship, ii) the limited observational constraint on this relationship in ERA20C, and iii) the unexplained²⁵ stronger global moistening in ERA20C compared to the same free-running numerical prediction model only driven by prescribed sea surface temperatures and radiative forcings²⁴.

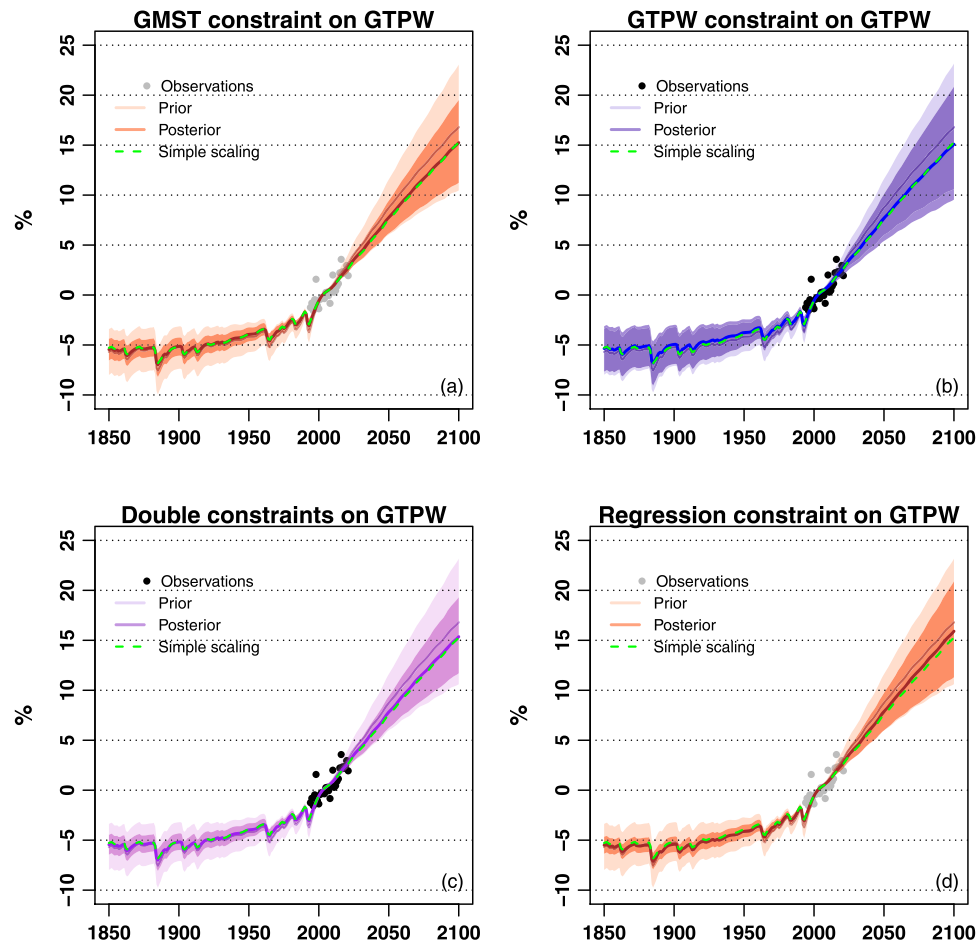


Fig. 3 Posterior versus prior distributions of forced changes in global mean total precipitable water. Mean (solid lines) and 5–95% range (shading) of the prior and posterior distributions of the forced GTPW annual mean response to both natural and anthropogenic radiative forcings in historical simulations and SSP2–4.5 projections from 28 CMIP6 models: **a** KCC using the GMST-only observational constraint; **b** KCC using the GTPW-only observational constraint; **c** KCC using both observational constraints; **d** Regression based on the GSAT posterior distribution and an observed 7%/°C regression coefficient as derived from GNSS and GMST observations (see text). After the constraint, the 5–95% interval at the end of the 21st century is reduced by 34%, 10%, 39% and 23% in panel a, b, c, and d respectively. In all panels, the dashed green line shows the ensemble mean GTPW change estimated when applying a simple scaling (see Methods) of the ensemble mean forced GSAT response. The mean observed anomalies are shown as black (gray) filled circles when they are (not) used for constraining the model response.

Recently, an original statistical method inspired by data assimilation has been developed to narrow uncertainty on simulated estimates of past and future human-induced global warming²⁷, as estimated from the increase in global mean surface air temperature (GSAT). The method has also been used at the regional scale²⁸ and tested successfully in a perfect model framework^{27,28}. This robust statistical approach called KCC (Kriging for Climate Change) uses CMIP projections to provide a prior of the real-world forced response and then derive the posterior of this response given the historical observations (see Methods). Model uncertainty is fully considered and the entire observational record is used to constrain past and future responses to natural and anthropogenic forcings in a consistent way. Moreover, the method has been enriched in order to enable the use of two observational constraints while accounting for their potential co-variability²⁸. Here, we consider constraints by global mean surface temperature (hereafter GMST, a blending of surface air temperature measured over land and of sea surface temperature measured over the oceans, which can be considered as good surrogates for GSAT) and/or by global mean estimates of total-column water vapour (GTPW) from GNSS and three reanalyses respectively.

Constraining the projected GTPW response using KCC (Fig. 3) leads to a substantial narrowing of the posterior compared to the prior distribution. Note that KCC only aims at constraining the forced GTPW response. Unlike more empirical emergent constraints^{16,29}, the method thus explicitly discards the contribution of internal climate variability. The constraint is first based either on GMST observations since 1850 (Fig. 3a) or on GTPW observations since 1994 (Fig. 3b). In sharp contrast with the regression technique (Supplementary Fig. 1d), KCC leads to a downward shift of the ensemble mean response, together with a reduction of the 5–95% confidence interval by 34% and 10% respectively. Combining the two observational constraints (Fig. 3c) shows that they are not fully redundant (despite the full consideration of their co-variability) since the posterior distribution is then narrowed by up to 39% at the end of the 21st century. All constraints lead to a posterior ensemble mean forced response that is very close to the rate obtained after applying a simple CC scaling of 7%/°C to the ensemble mean posterior estimate of the forced GSAT response.

This rate of 7%/°C is also consistent with the best estimate of both observed and KCC-constrained trends over recent decades (Fig. 4). The KCC results clearly show that all CMIP6 models do

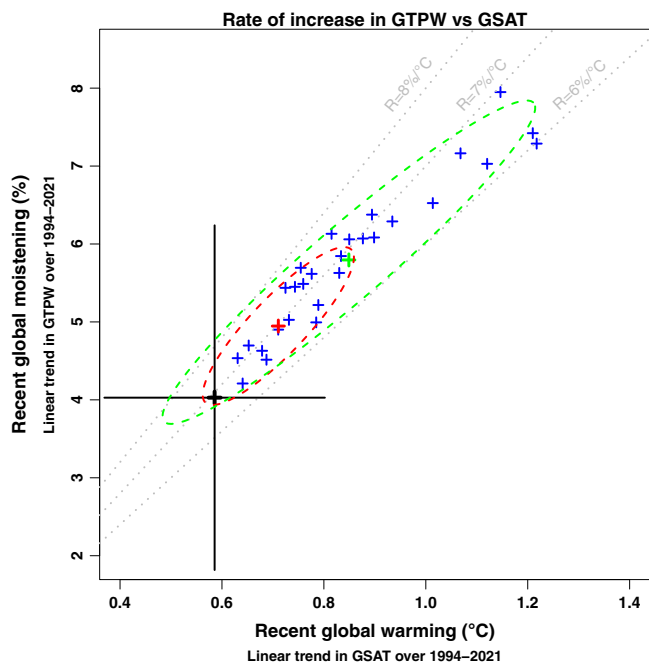


Fig. 4 Scatterplot of recent trends in global mean total precipitable water versus global mean surface air temperature. Linear trends in GTWP (%) versus corresponding trends in GSAT (K) over the 1994–2021 period where both observed estimates of GMST and GTPW are available. Individual CMIP6 models are shown as blue crosses while the ensemble mean and ensemble spread of their *prior* and *posterior* distributions are shown as crosses and ellipses in green and red respectively. Observed trends and related uncertainties are shown in black. The grey dotted lines denote three illustrative rates of increase ranging from 6%/°C to 8%/°C.

not agree with this best estimate. From 1994 to 2021, the unconstrained 5–95% confidence interval of the rate of increase in GTPW ranges from 6.2%/°C to 7.8%/°C, while the constrained confidence interval is between 6.5%/°C and 7.6%/°C, with a median value of 7.0%/°C. KCC also indicates that the GTPW and GMST observational constraints are quite redundant given the strong relationship between GSAT and GTPW trends across the CMIP6 models. Yet, the non-negligible inter-model spread in the rate of increase in GTPW as a function of global warming explains why the observational constraint from the GNSS measurements (and from global reanalyses) can represent an added-value compared to the use of GMST only. It is therefore important to maintain the GNSS network, which will be increasingly useful to constrain the projections of GTPW.

Given the much longer GMST record compared to the four GTPW datasets, an alternative strategy could consist in combining the KCC method, to constrain the GSAT response only, and the simple regression technique, to derive the forced GTPW response from the constrained forced GSAT response. Unlike in Supplementary Fig. 1d, the regression is now based on the GMST-constrained forced GSAT response (via KCC) rather than the full GSAT anomalies. A best-guess regression coefficient of 7.0%/°C, derived from the GMST and GNSS annual mean anomalies over the 1994–2021 overlapping period, is now applied to each CMIP6 model. This regression method is however less powerful than KCC for constraining the projections (Fig. 3d). This is due to a weak anti-correlation between the GSAT response and the rate of increase in GTPW across the CMIP6 models (Supplementary Fig. 2d).

The ensemble mean results of KCC provide an unequivocal demonstration that anthropogenic global warming occurs at

near-constant relative humidity. Further exploration of the behaviour of individual CMIP6 models at the end of the 21st century (Supplementary Fig. 2c) shows that all models project an exponential rate of increase of GTPW that is around 7%/°C when normalized by the corresponding increase in GSAT. The ensemble-mean rate of increase (6.95%/°C) is similar in CMIP5 models (not shown), but hides some model disparity with extreme values of 6.1%/°C and 7.9%/°C respectively. Note that there is no reason why the rate of increase should be exactly 7%/°C after averaging both precipitable water and surface temperature at the global scale. For instance, deviations from CC scaling of zonal-mean rather than global-mean precipitable water has been shown to result from decreases in relative humidity in the subtropics and mid-latitudes, and increases in the deep tropics⁶. Our subset of CMIP6 models projects a maximum absolute increase in precipitable water in the tropics (Supplementary Fig. 3a), where contrasted temperature biases³⁰ may contribute to the inter-model spread in the estimated moistening rates given the sensitivity of the CC relationship to the background temperature. In contrast, the relative increase in precipitable water (Supplementary Fig. 3b) is maximum in the polar latitudes, but should not much contribute to the inter-model spread in GTPW changes given the much lower absolute values of specific humidity. Further investigation is however needed to identify the latitudes or regions that contribute the most to the inter-model spread. Changes in the vertical profiles of temperature and specific humidity should be also explored³¹, including in the tropical upper troposphere where the model response to global warming was shown to be closely related to the model climatology³².

A potential weakness of the present study is the simple use of a single realization of the historical experiment and corresponding SSP2-4.5 scenario for each CMIP6 model. However, the use of at least three members (but only 19 instead of 28 models) leads to consistent results (Supplementary Fig. 4). Parallel computations have been also made using the SSP5-8.5 scenario from CMIP6 (Supplementary Fig. 5) or the RCP8.5 scenario from CMIP5 (Supplementary Fig. 6). Again, the KCC method leads to a narrowing and downward shift of the *posterior* distribution compared to the *prior*, with an ensemble mean response fully consistent with the CC relationship. Yet, the regression technique is more efficient with the CMIP5 models that do not show the previously discussed anti-correlation between the rate of increase in GTPW per °C and the GSAT response.

Conclusions

To sum up, the KCC statistical package has allowed us to constrain the climate projections of GTPW using two observational constraints, without assuming any analytical relationship between GTPW and GSAT, and taking account of both model and observational uncertainties. The resulting narrowing of the 5–95% confidence interval in the forced GTPW response is robust and found in two scenarios and two generations of GCMs. The KCC method also reduces the ensemble mean response, which then matches a 7%/°C rate of increase and provides further evidence of a human-caused global warming at near-constant tropospheric relative humidity. This finding is also supported by the D&A experiments from CMIP6, which show a consistent historical moistening dominated by GHG emissions but damped by anthropogenic aerosols over much of the 20th century. Interestingly, KCC is also useful to constrain the historical GTPW response to individual radiative forcings (Supplementary Fig. 7). While the opposite response to GHG versus anthropogenic aerosols (Fig. 2) is confirmed, KCC suggests that the over-estimation of the projected increase in GTPW is associated with a too strong sensitivity to both GHG and aerosols. This result

highlights the possible adverse effect of model tuning: the model ability to capture observed changes is not a full guarantee to provide reliable projections if the relative contributions of GHG and aerosol forcings vary in time or have not been correctly estimated over the historical period³³. Finally, the potential of the KCC method heavily relies on the availability of perennial and reliable observations that should be carefully maintained in order to document the multiple facets of climate change.

Methods

Observations and atmospheric reanalyses. The ground-based GNSS total-column water vapour (or total precipitable water) data used in this work are based on a homogeneous reprocessing of a global network of 434 GNSS stations for the period 1994–2014, extended with a consistent operational processing solution for the period 2015–2021. The basic GNSS product is the Zenith Tropospheric Delay available with a temporal sampling of 2 h. The data were thoroughly quality-checked and converted to total precipitable water using ERA5 6-hourly pressure level data, with high horizontal resolution (0.25°x0.25°), and aggregated to daily and monthly values. More information on the data processing and conversion can be found in ref. 20 (Bock, 2022). The global average time series shown in Fig. 1 includes 237 representative sites with more than 10 years of observations. Gaps in the GNSS time series were filled with ERA5 values to insure consistent temporal representativeness. Some differences with the reanalyses shown in Fig. 1 can arise from spatial representativeness differences as the reanalyses are full global averages. These reanalyses differ in the type of observations assimilated: ERA20C assimilates only surface pressure and marine wind observations, while ERA5, JRA55, and MERRA-2 assimilate a huge amount of conventional and satellite data (millions per day). Finally, a recent update of the HadCRUT5 dataset, covering the 1850–2021 period, is used to constrain the evolution of the global mean surface air temperature (GSAT). This dataset is a blending of surface air temperature measured over land and of sea surface temperature measured over the oceans (hereafter called GMST). While the AR6 suggested that the increase in GSAT is slightly higher than in GMST over the historical period, such a limited difference is not reliable across multiple CMIP6 models so that no correction has been here applied to compare the simulated GSAT with the observed GMST.

CMIP5 and CMIP6 multi-model ensembles. We make use of a large set of global climate models from both CMIP5 and CMIP6. We took all models providing at least one historical simulation and a corresponding scenario (SSP2-4.5 and SSP5-8.5 for CMIP6, only RCP8.5 for CMIP5) for both *tas* and *prw* monthly mean variables, corresponding to near-surface air temperature and total precipitable water respectively. As a result, we considered twenty-eight CMIP6 models for the SSP2-4.5 intermediate emission scenario (ACCESS-CM2, ACCESS-ESM-1-5, BCC-CSM2-MR, CanESM5, CESM2-WACCM, CNRM-CM6-1, CNRM-CM6-1-HR, CNRM-ESM2-1, EC-Earth3, EC-Earth3-CC, EC-Earth3-Veg, EC-Earth3-Veg-LR, FGOALS-g3, GFDL-CM4, GFDL-ESM4, GISS-E2-1-G, HadGEM3-GC31-LL, INM-CM4-8, INM-CM5-0, IPSL-CM6A-LR, KACE-1-0, MIROC-ES2L, MIROC6, MPI-ESM1-2-HR, MPI-ESM1-2-LR, MRI-ESM2-0, NorESM2-MM, UKESM1-0-LL), and two more models (HadGEM3-GC31-MM and NorESM2-LM) for the SSP5-8.5 high-emission scenario. Alternatively, we also used a subset of nineteen CMIP6 models with at least three realizations. For the detection-and-attribution analysis, we considered a smaller subset of eight CMIP6 models (ACCESS-ESM-1-5, BCC-CSM2-MR, CanESM5, CNRM-CM6-1, GFDL-ESM4, HadGEM3-GC31-LL, IPSL-CM6A-LR, MRI-ESM2-0) providing at least three realizations for the following four experiments: hist-ALL (historical simulations with all natural and anthropogenic forcings), hist-GHG (simulations driven by evolving GHG concentrations only), hist-AER (simulations driven by evolving anthropogenic aerosol loadings only), and hist-NAT (simulations driven by evolving solar and volcanic forcings only). Historical simulations and the corresponding RCP8.5 high-emission scenario from twenty-eight CMIP5 models (bcc-csm1-1-m, BNU-ESM, CanESM2, CCSM4, CESM1-CAM5, CMCC-CM, CMCC-CMS, CNRM-CM5, CSIRO-Mk3-6-0, FIO-ESM, GISS-E2-H, GISS-E2-H-CC, GISS-E2-R, GISS-E2-R-CC, HadGEM2-ES, Inmcm4, IPSL-CM5A-LR, IPSL-CM5A-MR, IPSL-CM5B-LR, MIROC5, MIROC-ESM, MIROC-ESM-CHEM, MPI-ESM-LR, MPI-ESM-MR, MRI-CGCM3, MRI-ESM1, NorESM1-M, NorESM1-ME) have been also used. All model outputs have been retrieved from the IPSL ESPRI platform (<https://mesocentre.ipsl.fr/plate-forme-physique/>). Annual mean anomalies have been estimated relative to the 1995–2014 baseline reference period.

The simple CC scaling. The objective is to derive changes in GTPW from changes in GSAT. Inspired by the Clausius-Clapeyron (CC) relationship, this scaling is obtained by regressing the annual mean anomalies of $\ln[\text{GTPW}]$ onto the corresponding annual mean anomalies of GSAT. The assumption of an exponential dependence of GTPW on temperature is not quite correct for finite rather than small changes in GSAT⁵ and for global mean rather than local values, but it is assumed to be adequate to capture the leading-order sensitivity of GTPW to GSAT.

This scaling means that we do not use a linear rate to characterize the relative increase in GTPW per 1 °C of global warming, but rather an exponential rate as previously proposed to quantify relative changes in the intensity of daily precipitation extremes⁵. This rate of increase is derived as follows:

$$R = (\Delta\text{GTPW}/\text{GTPW} + 1)^{1/\Delta\text{GSAT}} - 1 \quad (1)$$

where $\Delta\text{GTPW}/\text{GTPW}$ denotes the fractional changes in GTPW and ΔGSAT denotes the GSAT anomalies. Note that we do not account for uncertainties in the coefficient of the linear regression $\ln[\Delta\text{GTPW}] \sim \Delta\text{GSAT}$ when we use this regression to predict changes in GTPW.

The KCC (Kriging for Climate Change) statistical method. The observational constraint method, called Kriging for Climate Change (KCC), has been previously applied to global mean warming²⁷ and regional warming²⁸, and can be easily derived for other climate variables. As explained in these seminal studies, this technique consists of three steps. First, the forced response of each climate model is estimated over the whole 1850–2100 period (after concatenation of historical simulations with corresponding 21st century projections). In order to also get attribution statements, the responses to ALL (all forcings), NAT (natural forcings only) and GHG forcings are estimated separately. Second, the sample of the forced responses from available climate models is used as a *prior* of the real-world forced response, assuming that “models are statistically indistinguishable from the truth”. Third, observations are used to derive a *posterior* distribution of the past and future forced response given observations.

This Bayesian method can be summarised using the following equation:

$$y = Hx + \varepsilon \quad (2)$$

where y is the time-series of observations (a vector), x is the time-series of the forced response (a vector), H is an observational operator (matrix), ε is the random noise associated with internal variability and measurement errors (a vector), and $\varepsilon \sim N(0, \Sigma_\varepsilon)$, where N stands for the multivariate Gaussian distribution. Climate models are used to construct a *prior* on x : $\pi(x) = N(\mu_x, \Sigma_x)$. Then the *posterior* distribution given observations y can be derived as $p(x|y) = N(\mu_p, \Sigma_p)$. Remarkably, μ_p and Σ_p are available in closed-form expressions.

In the following, we assess the forced response of annual and global mean total precipitable water (GTPW), as well as the response to specific subsets of radiative forcings (attribution). These forced responses are then constrained by GMST (a good surrogate for GSAT) and/or by observations and reanalyses of GTPW.

Therefore, we consider the following CMIP matrix:

$$x = (T_{all}, W_{all}, W_{ghg}, W_{nat}) \quad (3)$$

where each element is an entire 1850–2100 time-series of the forced response, T and W stand for GSAT and GTPW, respectively. “all”, “ghg” or “nat” are the subsets of external forcings considered. Similarly, we define an observed matrix as:

$$y = (T_{obs}, W_{obs}) \quad (4)$$

i.e., only observed time-series are used in y (1850–2021 for GMST, 1994–2021 for GTPW). As a result, x is a very long vector, and all attribution or projection diagnoses presented below can be derived from the *posterior* distribution $p(x|y)$. μ_x and Σ_x are estimated as the sample mean and covariance of the forced responses. Σ_y requires statistical modelling of internal variability and measurement errors, and we use a mix of auto-regressive processes of order 1 (AR1) to model internal climate variability. The intrinsic variance of both GMST and GTPW is derived from observations after subtracting the multi-model mean estimate of the forced response of GSAT and GTPW respectively. We also assume a dependence between GMST and GTPW internal variability, by accounting for the correlation between the two residuals in Σ_y . The assessment of measurement uncertainty is based on the HadCRUT5 ensemble for GMST (200 members), while for GTPW, we use three global atmospheric reanalyses in addition to the in situ GNSS measurements: ERA5, JRA55 and MERRA-2.

Data availability

CMIP5 and CMIP6 data are available on the ESGF archive at <https://esgf-node.llnl.gov/>, GNSS data at <https://en.acris-data.fr/>, and HadCRUT5 data at <https://www.metoffice.gov.uk/hadobs/hadcrut5/>.

Code availability

The KCC statistical package for observational constraint is available on gitlab at <https://gitlab.com/saidqasmi/KCC>, scripts used to plot the figures are available upon request from the corresponding author.

Received: 2 May 2022; Accepted: 22 September 2022;

Published online: 10 October 2022

References

- Held, I. M. & Soden, B. J. Robust Responses of the Hydrological Cycle to Global Warming. *J. Climate* **19**, 5686–5699 (2006).
- Allan, R. P. et al. Advances in understanding large-scale responses of the water cycle to climate change. *Annals of the New York Academy of Sciences*, <https://doi.org/10.1111/nyas.14337> (2020).
- Douville, H., et al. In Climate Change 2021: The Physical Science Basis. *Contribution of Working Group I to the Sixth Assessment Report of the Intergovernmental Panel on Climate Change*. Chapter 8 (Cambridge University Press, 2021).
- Fischer, E. M. & Knutti, R. Observed heavy precipitation increase confirms theory and early models. *Nat. Clim. Change* **6**, 986–991 (2016).
- John, A., Douville H., Ribes A., Yiou P. CMIP6 model uncertainties in extreme precipitation projections. *Weather and Climate Extremes* (revised, 2022).
- O’Gorman, P. A. & Muller, C. J. How closely do changes in surface and column water vapor follow Clausius–Clapeyron scaling in climate change simulations. *Environ. Res. Lett.* **5**, 025207 (2010).
- Climate Change 2021: The Physical Science Basis. *Contribution of Working Group I to the Sixth Assessment Report of the Intergovernmental Panel on Climate Change* [Masson-Delmotte, V., et al. (eds.)]. Cambridge University Press (2021).
- Vial, J., Dufresne, J. L. & Bony, S. On the interpretation of inter-model spread in CMIP5 climate sensitivity estimates. *Clim. Dyn.* **41**, 3339–3362 (2013).
- Douville, H. et al. Drivers of the enhanced decline of land surface relative humidity in CNRM-CM6-1. *Clim. Dyn.* **5**, 1613–1629 (2020).
- Allan, R. P., Willett, K. M., John, V. O., Trent, T. Global changes in water vapor 1979–2020. *J. Geophys. Res.*, <https://doi.org/10.1029/2022JD036728> (2022).
- Schröder, M. et al. The GEWEX Water Vapor Assessment: overview and introduction to results and recommendations. *Remote Sens.* **11**, 25 (2019).
- Bosilovich, M. G., Robertson, F. R., Takacs, L., Molod, A. & Mocko, D. Atmospheric Water Balance and Variability in the MERRA-2 Reanalysis. *J. Climate* **30**, 1177–1196 (2017).
- Santer, B. D. et al. Identification of human-induced changes in atmospheric moisture content. *Proc. Nat. Am. Soc.* **104**, 15248–15253 (2007).
- Chung, E.-S., Soden, B., Sohn, B. J. & Shi, L. Upper-tropospheric moistening in response to anthropogenic warming. *Proc. Nat. Am. Sc.* **111**, 11636–11641 (2014).
- Willett, K. M., Gillett, N. P., Jones, P. D., Thorne, P. M. Attribution of observed surface humidity changes to human influence. *Nature*, **449**, <https://doi.org/10.1038/nature06207> (2007).
- Douville, H. & Plazzotta, M. Midlatitude summer drying: An underestimated threat in CMIP5 models? *Geophys. Res. Lett.* **44**, 9967–9975 (2017).
- Dunn, R. J. H., Willett, K. M., Ciavarella, A. & Stott, P. A. Comparison of land surface humidity between observations and CMIP5 models. *Earth Syst. Dynam.* **8**, 719–747 (2017).
- Eyring, V., et al. In Climate Change 2021: The Physical Science Basis. *Contribution of Working Group I to the Sixth Assessment Report of the Intergovernmental Panel on Climate Change*. Chapter 3, (Cambridge University Press 2021).
- Bevis, M. et al. GPS Meteorology: Mapping zenith wet delay onto precipitable water. *J. Appl. Meteor.* **33**, 379–386 (1994).
- Bock, O. & Parracho, A. C. Consistency and representativeness of integrated water vapour from ground-based GPS observations and ERA-Interim reanalysis. *Atmos. Chem. Phys.* **19**, 9453–9468 (2019).
- Dow, J. M., Neilan, R. E. & Rizos, C. The International GNSS Service in a changing landscape of Global Navigation Satellite Systems. *J. Geod.* **83**, 191–198 (2009).
- Paracho, A. C., Bock, O. & Bastin, S. Global IWV trends and variability in atmospheric reanalyses and GPS observations. *Atmos. Chem. Phys.* **18**, 16213–16237 (2018).
- Bock, O. Global GNSS Integrated Water Vapour data, 1994–2021 [Data set]. AERIS. <https://en.aeris-data.fr/landing-page/?uuid=df7cf172-31fb-4d17-8f00-1a9293eb3b95> (2022).
- Poli, P. et al. ERA-20C: An Atmospheric Reanalysis of the Twentieth Century. *Journal of Climate* **29**, 4083–4097 (2016).
- Gillett, N. P. et al. Detection and Attribution Model Intercomparison Project (DAMIP). *Geosci. Model Dev. Discuss.* **9**, 3685–3697 (2016).
- Liepert, B. et al. Can aerosols spin down the water cycle in a warmer and moister world? *Geophys. Res. Lett.* **31**, L06207 (2004).
- Ribes, A., Qasmi, S. & Gillett, N. Making climate projections conditional on historical observations. *Sc. Adv.* **7**, eabc0671 (2021).
- Qasmi, S., Ribes, A. Reducing uncertainty in local climate projections. *Sc. Adv.*, preprint, <https://doi.org/10.21203/rs.3.rs-364943/v3> (2022).
- Knutti, R. et al. A climate model projection weighting scheme accounting for performance and interdependence. *Geophys. Res. Lett.* **44**, 1909–1918 (2017).
- Han, Y., Zhang, M.-Z., Xu, Z. & Guo, W. Assessing the performance of 33 CMIP6 models in simulating the large-scale environmental fields of tropical cyclones. *Clim. Dyn.* **58**, 1683–1698 (2022).
- Trent, T., Schröder, M. & Remedios, J. GEWEX water vapor assessment: Validation of AIRS tropospheric humidity profiles with characterized radiosonde soundings. *Journal Geophys. Res.: Atmos.* **124**, 886–906 (2019).
- Po-Chedley, S., Zelinka, M. D., Jeevanjee, N., Thorsen, T. J. & Santer, B. D. Climatology explains intermodel spread in tropical upper tropospheric cloud and relative humidity response to greenhouse warming. *Geophys. Res. Lett.* **46**, 13,399–13,409 (2019).
- Moseid, K. O. et al. in CMIP6 models as compared to observed regional dimming and brightening. *Atmos. Chem. Phys.* **20**, 16023–16040 (2020). no. 24.

Acknowledgements

The authors are grateful to all global modelling centres which have contributed to CMIP5 and CMIP6, as well as to the people in charge of the ESGF archive (<https://esgf-node.llnl.gov/projects/>) and of the ESPRI platform (<https://mesocentre.ipsl.fr/plate-forme-physique/>). The study has been partly supported by the European Union’s Horizon 2020 research and innovation program under the EUCP (Grant Agreement 776613) and the CONSTRAIN (Grant Agreement 820829) projects.

Author contributions

H.D. designed the research, processed the CMIP5 and CMIP6 datasets, produced all figures except Fig. 1 and drafted the first manuscript; O.B. processed the GNSS measurements and the atmospheric reanalyses and produced Fig. 1; A.R. and S.Q. developed the KCC statistical packages, everyone participated in the writing of the submitted manuscript.

Competing interests

The authors declare no competing interests.

Additional information

Supplementary information The online version contains supplementary material available at <https://doi.org/10.1038/s43247-022-00561-z>.

Correspondence and requests for materials should be addressed to Hervé Douville.

Peer review information *Communications Earth & Environment* thanks Kate Willett and the other, anonymous, reviewer(s) for their contribution to the peer review of this work. Primary Handling Editors: Clare Davis and Heike Langenberg. Peer reviewer reports are available.

Reprints and permission information is available at <http://www.nature.com/reprints>

Publisher’s note Springer Nature remains neutral with regard to jurisdictional claims in published maps and institutional affiliations.



Open Access This article is licensed under a Creative Commons Attribution 4.0 International License, which permits use, sharing, adaptation, distribution and reproduction in any medium or format, as long as you give appropriate credit to the original author(s) and the source, provide a link to the Creative Commons license, and indicate if changes were made. The images or other third party material in this article are included in the article’s Creative Commons license, unless indicated otherwise in a credit line to the material. If material is not included in the article’s Creative Commons license and your intended use is not permitted by statutory regulation or exceeds the permitted use, you will need to obtain permission directly from the copyright holder. To view a copy of this license, visit <http://creativecommons.org/licenses/by/4.0/>.

© The Author(s) 2022